The International Journal of Advanced Manufacturing Technology (2018) 95:3215–3225
https://doi.org/10.1007/s00170-017-1412-9

ORIGINAL ARTICLE

Effect of root pass filler metal on microstructure and mechanical properties in the multi-pass welding of duplex stainless steels

Ahmed Kellai[1,2] · Azzedine Lounis[1] · Sami Kahla[2] · Brahim Idir[2]

Received: 27 August 2017 / Accepted: 14 November 2017 / Published online: 8 December 2017

Abstract
This paper is focused on the estimation of the effect of root pass chemical composition, in multi-pass GTA Weldments, on microstructure and mechanical properties of duplex stainless steel welds. We used two different filler metals, the super duplex ER 2594 and duplex ER 2209. Microstructures of different passes of welded joints are investigated using optical microscope and scanning electron microscope. The relationship between mechanical properties, corrosion resistance, and microstructure of welded joints is evaluated. It is found that the tensile and toughness properties of the first weldment, employing the combination of ER 2594 in the root pass and ER 2209 in the remaining, are better than that of the second weldment employing ER 2209 all passes, due to the root pass grains refinement and its alloy elements content as chromium Cr and nitrogen N. The microstructure indicates the presence of austenite in different forms on the weld zone of ER 2209, same in the case of ER 2594, but with higher content and finer grains size, in particular Widmanstätten austenite WA. Potentiodynamic polarization tests of the first weld metal evaluated in 3.5% NaCl solution at room temperature have been demonstrated a corrosion resistance higher than that of the second weld metal. This work addressed the improvement of the corrosion resistance using appropriate filler metal without getting any structural heterogeneity and detrimental changes in the mechanical properties.

Keywords Gas tungsten arc welding (GTAW) · Duplex stainless steel · Root pass · Filler metal · Microstructure and mechanical properties

1 Introduction

The use of combination between duplex and super duplex filler materials to produce a standard duplex stainless steel weld becomes an industrial necessity, especially when a highest corrosion resistance is required. The good weldability of duplex stainless steels, the right selection of welding parameters such as preheat, inter-pass temperature, shielding gas, heat input…, and the most appropriate choice of proper filler metal, will enable to obtain a desirable microstructure and mechanical characteristics of weldment.

The different grades of the duplex stainless steel (DSS) family (lean duplex 2304, standard grade 2205, super duplex 2507, and hyper duplex 2707) are determined according to alloy elements content and the corrosion resistance level [1, 2]. The duplex stainless steel has a wide range of applications, particularly in the construction of pipelines, which becoming increasingly recognized by the oil and gas industry. Its chemical composition which allows good proportion of austenite (γ)/ferrite (δ) in the vicinity of 1:1 offers superior mechanical and noticeable corrosion resistance in several aggressive environments [3–5].

The ferrite content and hence mechanical properties depends on the chemical composition in the weld metal, residual stress, and cooling rate, which are related to the heat input of welding process [6–8]. Low values of heat inputs lead to high

✉ Ahmed Kellai
kellai.a.a@gmail.com

Azzedine Lounis
zlounis@yahoo.com

Sami Kahla
samikahla40@yahoo.com

Brahim Idir
b.idir@crti.dz

[1] Laboratory of Sciences and Materials Engineering, LSGM, FGMGP, University of Sciences and Technology Houari Boumediene, BP 32 El Alia, Bab Ezzouar, 16111 Algiers, Algeria

[2] Research Center in Industrial Technologies, CRTI, P.O. Box 64, Cheraga, 16014 Algiers, Algeria

Table 1 Chemical composition of base metal and filler metals (wt.%)

Element		C	Mn	Si	S	P	Cr	Ni	Mo	Cu	Nb	N	Cr_{eq}/Ni_{eq}
Base metal	AISI 2205	0.015	1.13	0.49	0.0005	0.026	22.15	5.33	3.18	–	–	0.17	72.1
Filler metal	ER 2594	0.02	0.4	0.30	0.015	0.02	25.1	9.5	4.0	–	–	0.24	.169
	ER 2209	0.02	1.57	0.46	0.010	0.01	22.9	8.6	3.1	0.1	0.01	0.16	.180

ferrite contents and may promote Cr_2N precipitation. Otherwise, high values of heat inputs and low cooling rate at the temperature range of 1000–475 °C may help formation of fragile intermetallic phases such as σ and χ [9, 10]. These lead to the formation of different precipitates resulting in detrimental changes in the properties of the material, especially in its toughness [11], the addition of nitrogen significantly in the solid solutions delays their training [12–14].

The use of the duplex stainless is frequently limited to an upper and lower service temperature generally between −40 and 250 °C, where it has good mechanical properties better than ferritic and austenitic steel [15, 16]. At sub-zero temperatures the duplex stainless steels exhibit a ductile to brittle transition, where the ferrite becomes increasingly brittle [17]. The temperature for the ductile to brittle transition depends on the chemical composition and the ferrite phase content [11, 18]. The ferrite content increased as the Cr_{eq}/Ni_{eq} ratio increased [19]. The addition of nickel and nitrogen in the metal deposited leads to increase the impact toughness particularly at low temperature [20, 21]. In [7], it has also been lighted that the effect of the alloying elements on the ferrite/austenite ratio is much more important than the cooling rate.

The gas constructions are usually based on the use of duplex stainless steel pipes welded, and in order to avoid the corrosive effect of this gas inside these pipes, a super duplex filler metal is recommended to realize the root pass. For this reason, our contribution is a comparison between two welded pipes 2205 DSS. The first one is realized by using two different welding consumables; ER 2594 has the root pass and ER 2209 the remaining of the weld. The second one is realized by ER 2209 for all passes. This is to assess in detail the effect of chemical composition of deposit metal root pass on the microstructure, mechanical behavior, and corrosion resistance of different area of welding.

2 Materials and methods

An UNS 31803 grade duplex stainless steel in the form of pipe of 50.8 mm diameter and 5.54 mm thickness was considered. A multi-pass welding was performed using GTA welding process with the previous filler metals. The chemical composition of the base metal and filler metals is given in Table 1. The two welds are realized by the same qualified welder, who executes each pass carefully and following a welding procedure specification (WPS), established from qualification tests, containing well-defined welding parameters. The welding energy E (kj/mm) depends on the welding current (I), welding voltage (V), and welding speed S (mm/mn) by the following relation:

$$E = \frac{60^{*} I^{*} V}{S^{*} 1000} \quad (1)$$

The welding parameters used in this work are listed in Table 2. A radiographic test (RT) was performed on the welds, and it shows that the two joints are totally within whole types of welding defects.

Microscopic observations of the weld metal (WM), heat-affected zone (HAZ), and base metal (BM) in the welded joints are executed on cross sections to the welding direction, using standard techniques for mechanical polishing to obtain a mirror state. Then, the specimens were electrolytic etched in 10% KOH solution at 3 V for 20 s. The optical observations

Table 2 Welding parameters

Pass	Welding process	Wire diameter (mm)	Welding current (A)	Welding voltage (V)	Welding speed (mm/mn)	Welding energy (kj/mm)	Inter-pass temperature (°C)	Shielding gas (%)	Flow rate (l/min)
Root	GTAW	2.4	90–95	10–12	30–40	1.71–1.80	150	Ar99.999	12
Second	GTAW	2.4	115–120	10–12	60–80	1.08–1.15	150	Ar99.999	12
Filler	GTAW	2.4	100–110	10–12	40–50	1.50–1.58	150	Ar99.999	12
Cap	GTAW	2.4	100–110	10–12	40–50	1.50–1.58	150	Ar99.999	12

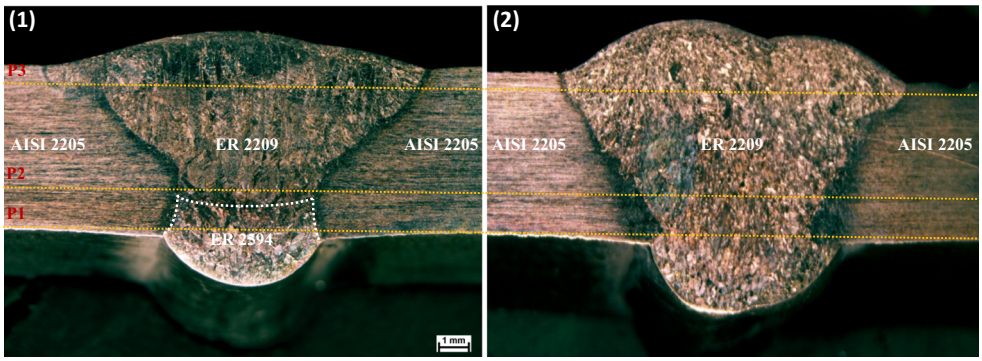

Fig. 1 Optical macrograph of the two welds joint

and also measurements of volume fractions of ferrite and austenite were performed using a light microscope (Nikon Eclipse LV100ND).

For the mechanical behavior, specimens testing are machined from the two welds; Charpy V-notch reduced specimens are prepared with dimensions of 5 × 10 × 55 mm in accordance with ASTM A370 standard. Impact tests were carried out at (20, 0, −20, −40, −60, −80 °C) for three locations that are (MB, WM1, and WM2) by means of a machine Charpy pendulum with 150 J impact load. The tensile test is carried out on the subsize specimens that are machined in accordance with ASTM E8-04 standard. The fracture surfaces after the test were captured by SEM observations. The electron microscope used was the ZEISS.EVO-MA 25 type coupled with microanalysis system (EDS). To see the effect of the root pass on the hardness profile (HV), the measures are taken across the weld joint according to three profiles P1, P2, and P3 as illustrated in Fig.1.

The corrosion behavior of welded joints is evaluated in solution of 3.5% sodium chloride (NaCl) at room temperature. Potentiodynamic polarization studies were conducted using Voltalab equipment (PGP 201). All experiments were performed by a conventional three-electrode cell, platinum foil as the auxiliary electrode and an Ag/AgCl as the reference one and samples as working electrode. Polarization curves were obtained after ½ h of exposure until obtaining a thermodynamic equilibrium, with a scan rate 1 mV/s.

3 Results and discussions

3.1 Microstructure

Figure 2 shows the micrographs of the base metal consisted of two-phase banded microstructure, where the elongated austenite (γ) phase is surrounded by the ferrite matrix (δ) along the rolling direction without any precipitates, the measured volume fraction of austenite and ferrite is average 47:53.

Generally, the solidification in DSS weld metals leads to ferrite and reformed austenite. The latter is the result of ferrite transformation during cooling, in which the austenite appears under different morphologies. In the first as grain boundary allotriomorphs (GBA) at the prior δ/δ grain boundaries at very high temperatures [4, 9, 20], as the cooling continues, the

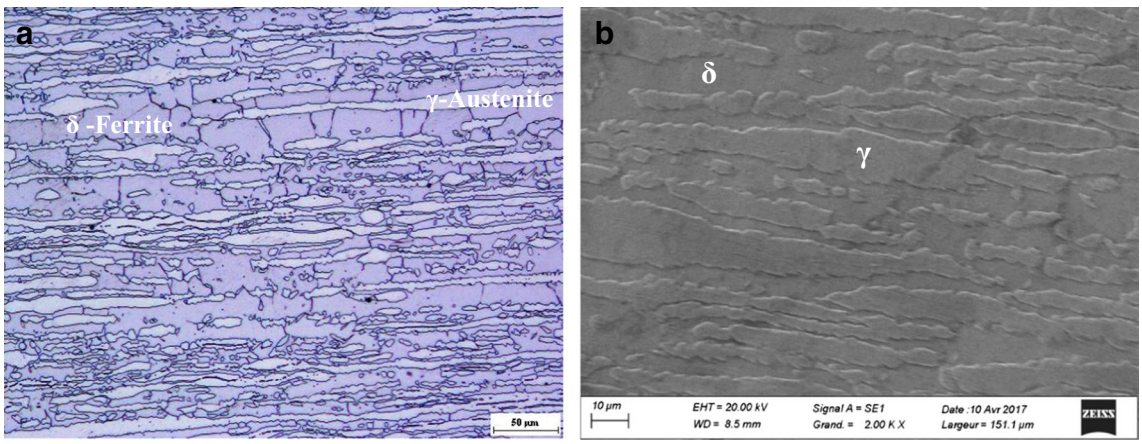

Fig. 2 Microstructure of BM in the as received condition. **a** Optical microscopy. **b** Scanning electron microscopy

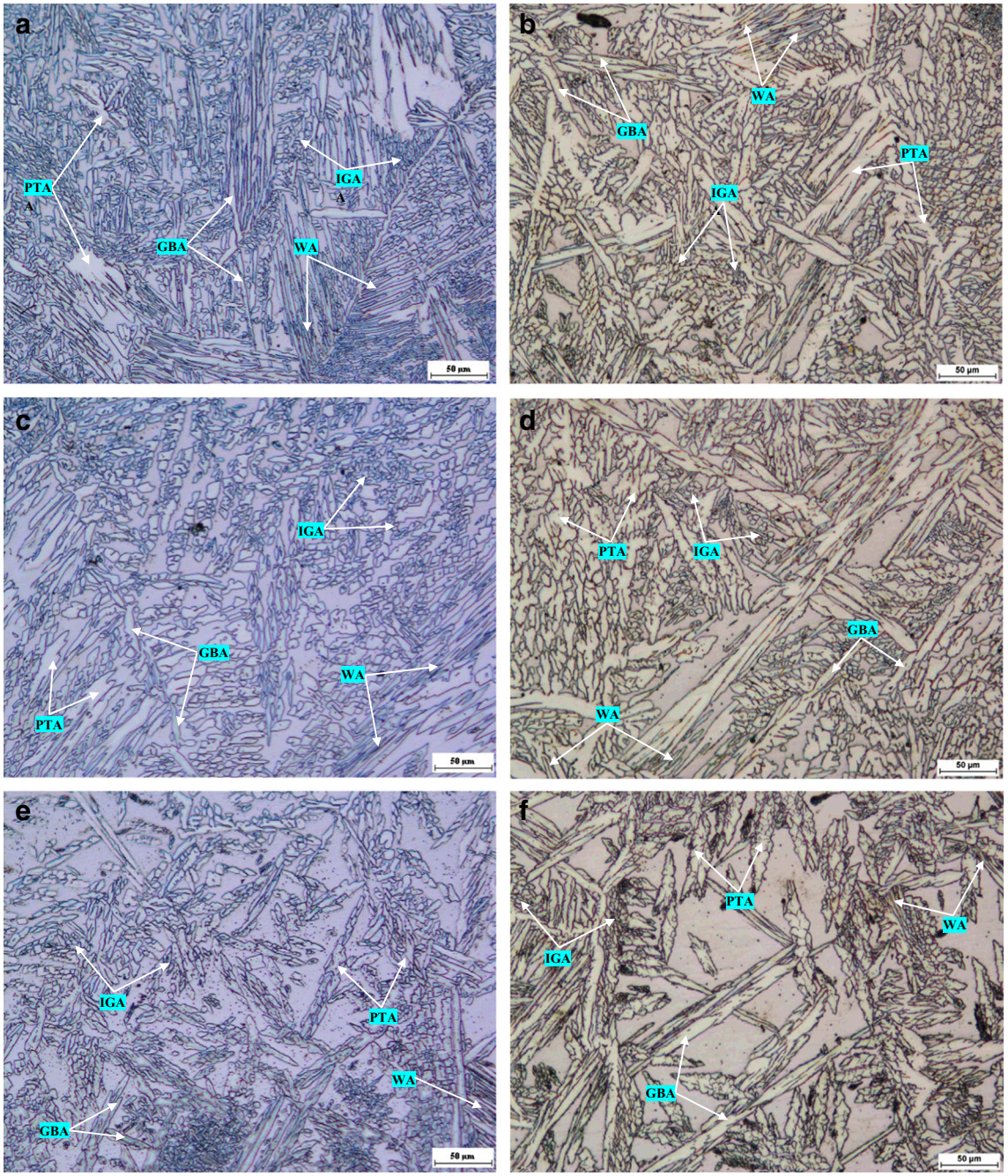

Fig. 3 Optical micrograph of the two welds metal. **a**, **b** Root pass. **c**, **d** Second pass. **e**, **f** cap

Widmanstätten side plates (WA) nucleated and grow into the grains from these allotriomorphs at the prior δ/δ or from partially transformed austenite (PTA) at δ/γ grain boundaries [4, 22], in the last the intragranular precipitates (IGA) within the δ ferrite matrix at low temperatures [7, 20].

According to [22], the cooling rate depends on heat input, preheating, thickness, welding speed, and chemical composition. As in our case, the welding conditions for the two welds are the same; the difference in cooling rate depends on the chemical composition of the filler metal. The amount of WA and IGA increased and the GBA coarsened much more at a much slower cooling rate [23] and as the nitrogen content is increased, the amount of austenite formed increases markedly, in particular Widmanstätten side plates and ferrite grain size become finer [20, 24, 25].

The microstructures of two deposited metals in each pass are shown in Fig. 3. The root pass of the first weld produced by ER 2594 filler metal (Fig. 3a) is completely different from the second weld (Fig. 3b). It is fine due to the high content of nickel and nitrogen [20], and it contains a large amount of reformed austenite of different morphologies, due to the high content of nitrogen which accelerates the reformation of

Table 3 Average compositions (%wt.) of the ferrite and austenite phases determined by EDS microanalysis

		γ-austenite				δ-ferrite			
	Location	Volume	Cr	Ni	Mo	Volume	Cr	Ni	Mo
Weld metal 1	Root pass	43.5 pct	24.85	9.35	3.45	56.5 pct	27.42	7.28	4.03
	Second pass	39.6 pct	24.79	9.14	3.67	60.4 pct	27.29	5.43	5.35
	Cap	35.1 pct	23.44	8.67	2.70	64.9 pct	24.55	7.00	4.19
Weld metal 2	Root pass	47.5 pct	22.33	9.17	2.61	52.5 pct	22.87	8.79	3.17
	Second pass	44.7 pct	21.95	9.04	2.55	55.3 pct	23.60	7.42	3.20
	Cap	35.4 pct	22.76	8.88	2.67	64.6 pct	23.14	7.26	4.02
Base metal		47 pct	22.03	6.43	2.81	53 pct	23.87	3.86	3.85

austenite during the cooling. There is also a small amount of PTA and fine ferrite grains. On the other hand, the root and second passes of the second weld are coarse with a high content of PTA (Fig. 3b and d).

The microstructure of the second pass of the first weld (Fig. 3c) is characterized by coarse austenite grains in particular IGA, due to the nitrogen diffusion from the root pass and low cooling rate [24], a small amount of WA and a relative increase of the ferrite content. Finally the cap pass undergoes a rapid cooling rate which leads to the increase of the ferrite content and becomes coarse with a little amount of reformed austenite (Fig. 3e and f). The austenite and ferrite volume fraction was determined in the different zones of the welds from image analysis (Table 3).

The HAZ contains mainly two sub-zones, the high temperature heat-affected zone HTHAZ (overheating zone) adjacent to the weld metal and the low temperature heat-affected zone LTHAZ (partially annealed zone) adjacent to the base metal [4, 26]. The HTHAZ can be defined as the zone next to the fusion boundary which approaches the melting point and will become almost completely ferritic on heating. In the HTHAZ zone, the temperature achieves very high values, around 1450 °C [9]. This temperature can also be predicted from the pseudo binary phase diagram of Fe–Cr–Ni system (Fig. 4). On cooling, the transformation $\delta \rightarrow \gamma$ is incomplete, hence high ferrite content is expected, so the austenite is reformed by solid-state transformation at the ferrite/ferrite boundaries and into the ferrite grains. The LTHAZ zone, where the temperature is between 800 and 1100 °C, is characterized by a small recrystallization of the microstructure which modified the grain morphology of the two phases. This light recrystallization is followed by a slight growth of the grains particularly those of the ferritic phase, so the percentage of austenite has been increased by 10% in comparison with the base metal [9, 12].

The differences between the HAZs are presented in the microstructures of Fig. 5a–c. As the nitrogen content in the deposited metals was decreased from 0.24 to 0.16 wt%, the size of the HTHAZ sub-zone and its ferrite content are increased, and the grain size of austenite is decreased [6, 25, 26]. The ferrite content is increased from 58 to 70% on average at the root pass and cap HTHAZ sub-zones respectively. In the second pass HTHAZ sub-zone where a mixture of two weld metals exists, a value of 65% on average is noted. There is not a great difference shown between the LTHAZ sub-zones, which are characterized by high amount of austenite, 46.5% on average. As a consequence, nitrogen limits the welding thermal effect and fosters austenite formation in the HAZ.

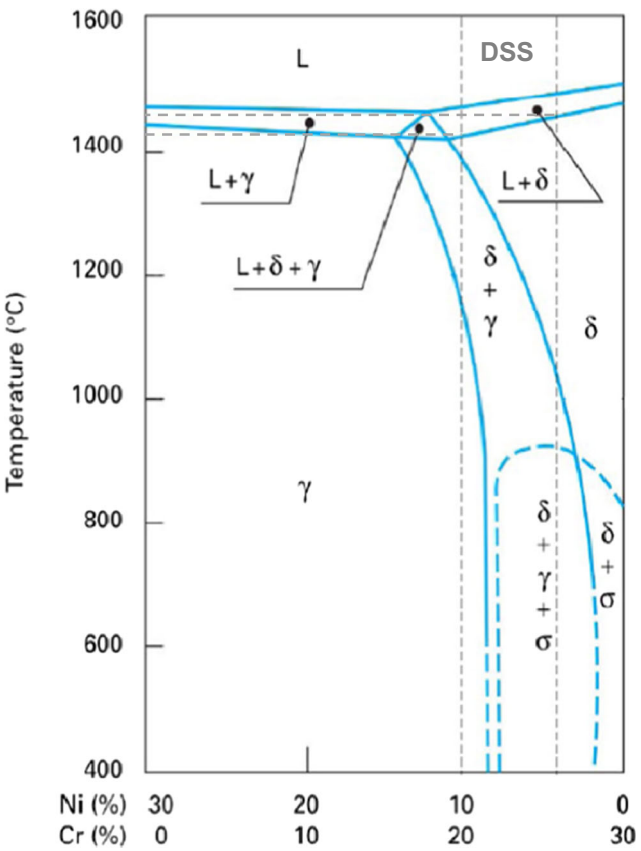

Fig. 4 Pseudo binary phase diagram of Fe–Cr–Ni system at equilibrium [7, 20]

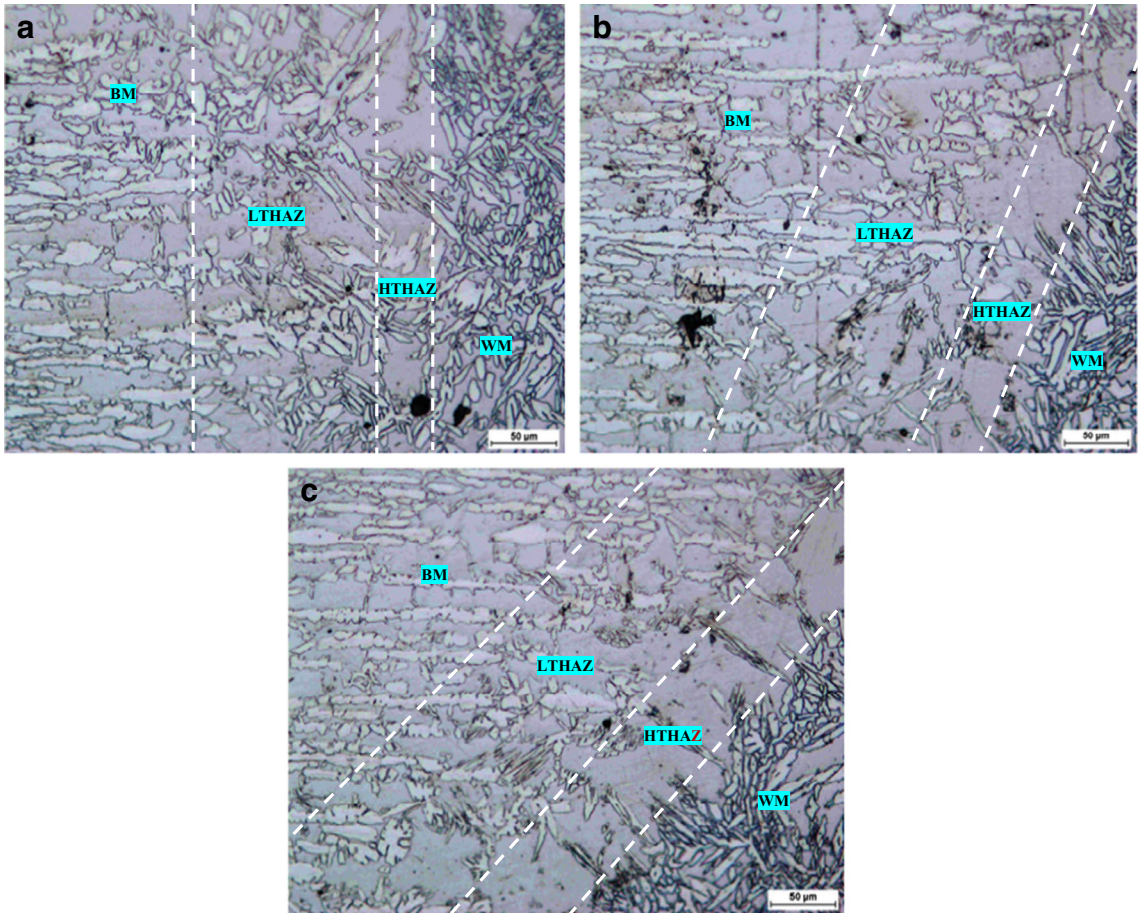

Fig. 5 Optical micrograph of fusion line at **a** root pass, **b** second pass, **c** cap in the first weld

3.2 SEM /EDAX analysis

Figure 6 shows the typical SEM/EDAX analysis in various areas for the two weld metals and the base metal, which indicates the different proportions of principal chemical elements. Table.3 summarizes the chromium, nickel, and molybdenum contents as a function of phase ferrite and austenite. It can be observed that nickel content is higher in the WM than in the BM because of the filler metals influence. It is clear that the amount of these chemical elements in the second pass of the first weld is almost the same as the root pass, which reveals the migration power of these elements in particular chromium

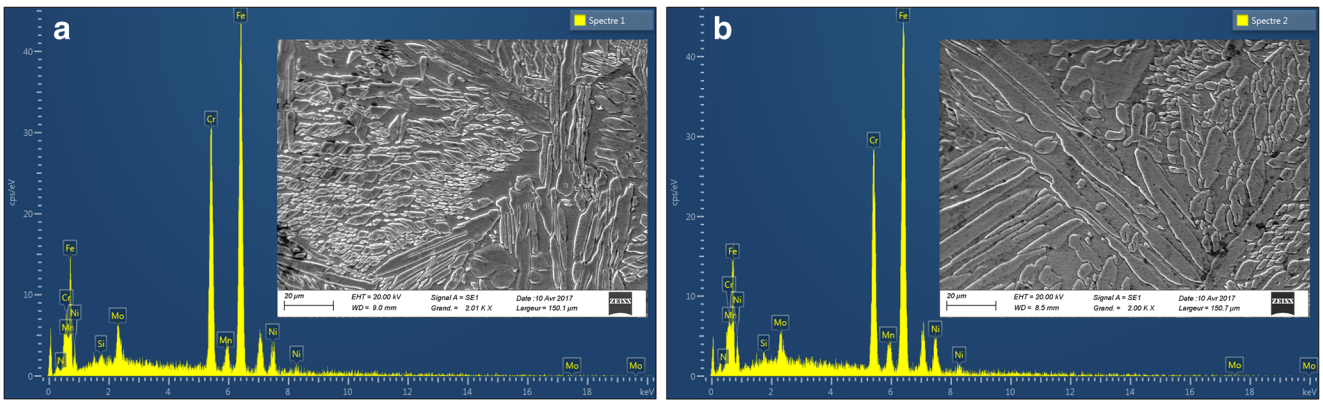

Fig. 6 Typical SEM/EDS spectrums for the root pass employing **a** ER 2594 and **b** ER 2209 filler

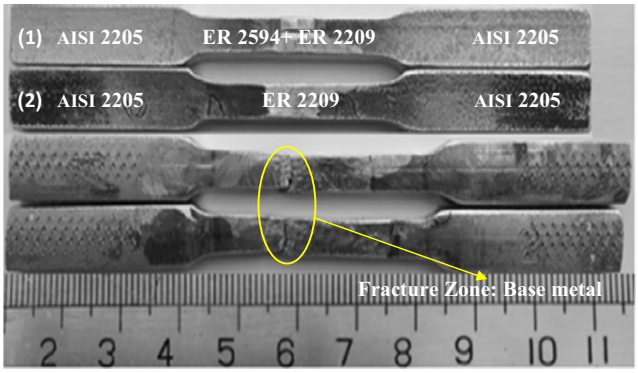

Fig. 7 Tensile photographs of the two weldments

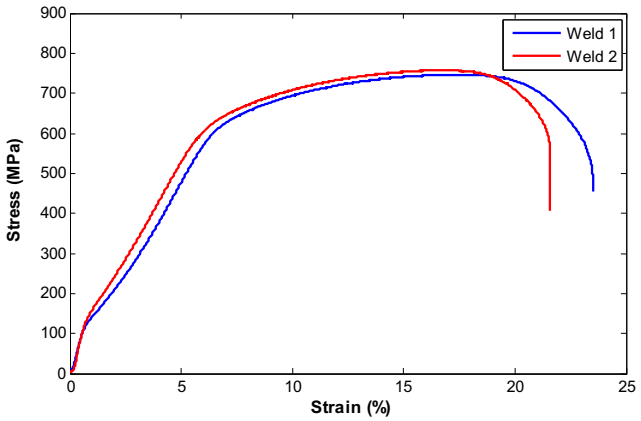

Fig. 8 The result of strength test for two weldments

[27]. It is also found that the austenite is characterized by a high level of nickel, which is the same for chromium and molybdenum in the ferrite. However, the volume fraction of this last is slightly higher in the root and second passes of first weldment, due to the increase of chromium content in the filler metal [19]. Phase proportion of deposited metal from root pass to cap was irregular due to different cooling rate and inter-pass dilution [22].

3.3 Mechanical properties

3.3.1 Tensile testing

The two weldments tensile test reveals that there is a fracture in the base metal (Fig.7). The tensile properties of the GTA weldments of DSS at 1 mm/min strain rate are reported in Table 4. From the stress strain curve (Fig. 8), the tensile strength value of the first weld (743.3 MPa) is found to be lower than that of the second weld (757.4 MPa). On the other hand, the ductility values are higher, due to the decrease of root pass grain sizes and the changes in the morphologies and proportions of austenite [27, 28].

3.3.2 Impact and fracture toughness testing

Figure 9 presents the toughness values of the BM, WM1, and WM2 under various temperatures. It is inferred that by decreasing the temperature, a reduction in impact toughness is recorded. The impact strength values of the WM1 are greater than that of the WM2, this might be due to the difference that exist between the ferrite content and the fine austenitic grains size in the root pass, but less than that of the base metal. This difference appears clearly for low temperatures from − 20 °C, due to the structural fragility induced by the various morphologies of austenite.

The fracture surfaces in the different areas of welds at 20 °C and −80 °C are illustrated in Fig. 10 and Fig. 11. It is known that the fracture mechanisms of duplex stainless steel weld materials are identified by its proper microstructure, which are the austenite dimple fracture was principal fracture mode [23, 29]. Concerned the first weld at 20 °C, the root pass exhibits a ductile fracture with narrow and deep dimples as in Fig. 10a. In the second pass, the dimples are medium sizes and deep (Fig. 10b). However, the cap dimples are more wide-shaped and shallow (Fig. 10c). Furthermore, the presence of voids in the fracture is observed for all passes in particular for cap. Also, it could be seen that the fractographs at − 80 °C (Fig. 10d–f) demonstrates a mixed mode of ductile and brittle fracture; this last highlights a small and discontinuous cleavage area. On the other hand, the fracture mode in the second weld shows a ductile appearance with large and shallow

Table 4 Tensile properties of the two weldments

Material	Ultimate tensile strength (MPa)	Yield strength 0.2% (MPa)	Elongation (%)
Weld 1	743.3	578.89	23.57
Weld 2	757.4	607.43	21.78

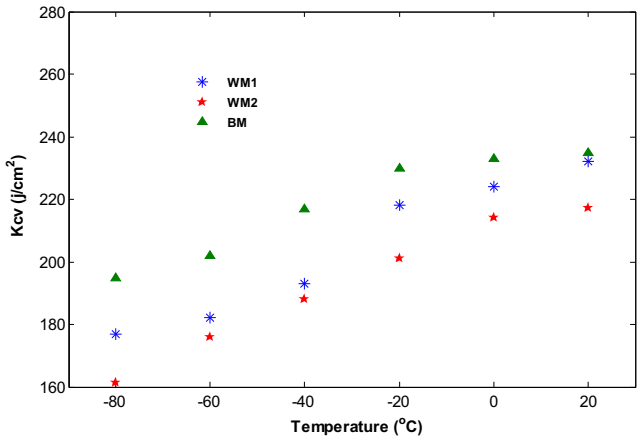

Fig. 9 The result of impact toughness for base metal and two weldments

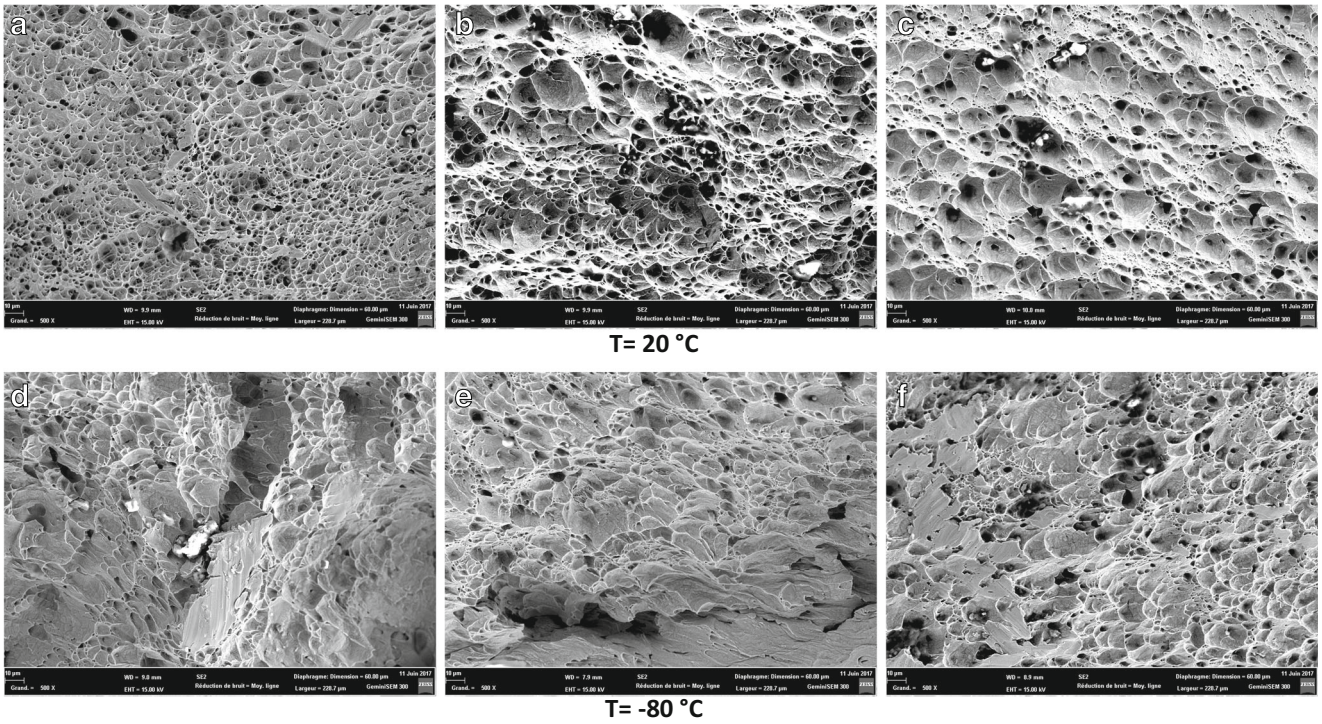

Fig. 10 SEM micrograph of the impact fractured in the WM1. **a**, **b** Root pass. **c**, **d** Second pass. **e**, **f** Cap

dimples plus banded ferrite (Fig. 11a and b). At − 80 °C, it can be noted a mixed mode characterized by elongated cleavage facets (Fig. 11d and e). The fracture of the base metal at room temperature revealed ductile mode (Fig. 11c). But in low temperature (− 80 °C) showed predominantly ductile fracture mechanism where large cleavage facets could be observed

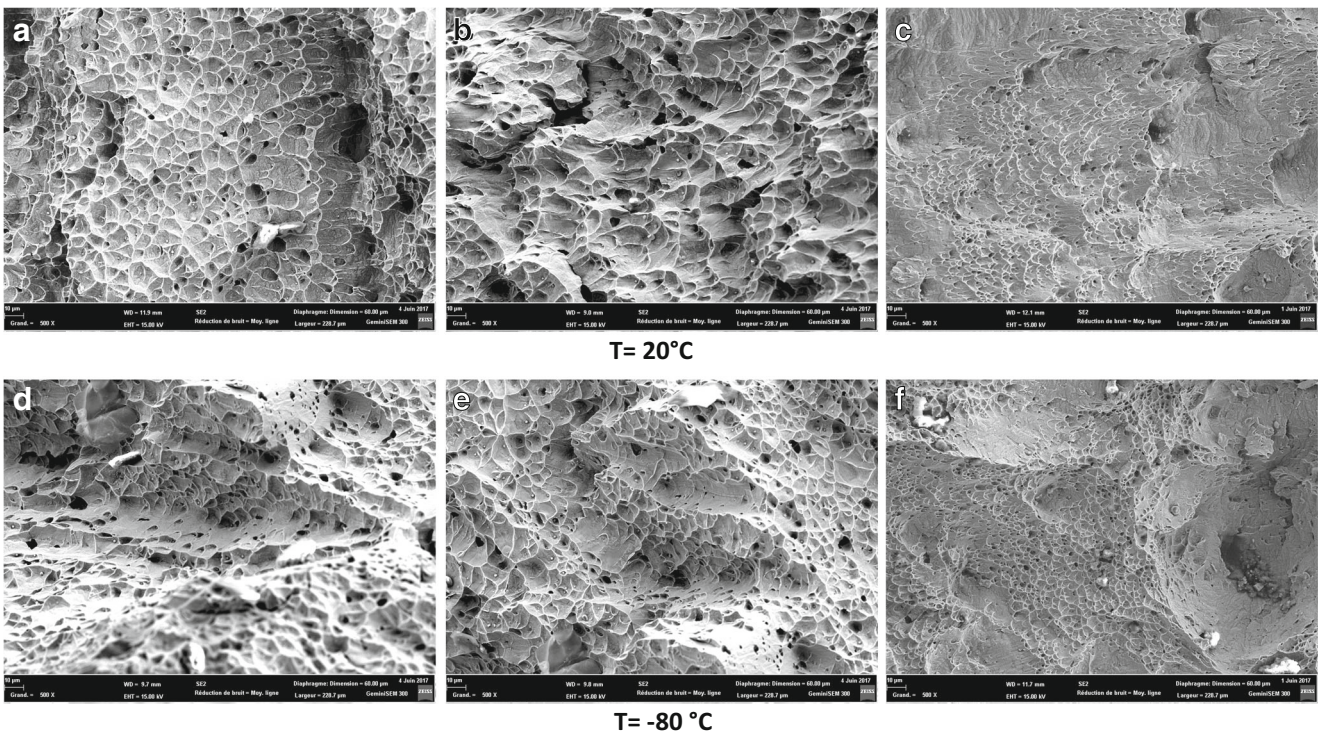

Fig. 11 SEM micrograph of the impact fractured in the WM2. **a**, **b** Root pass. **c**, **d** Second pass. **e**, **f** Base metal

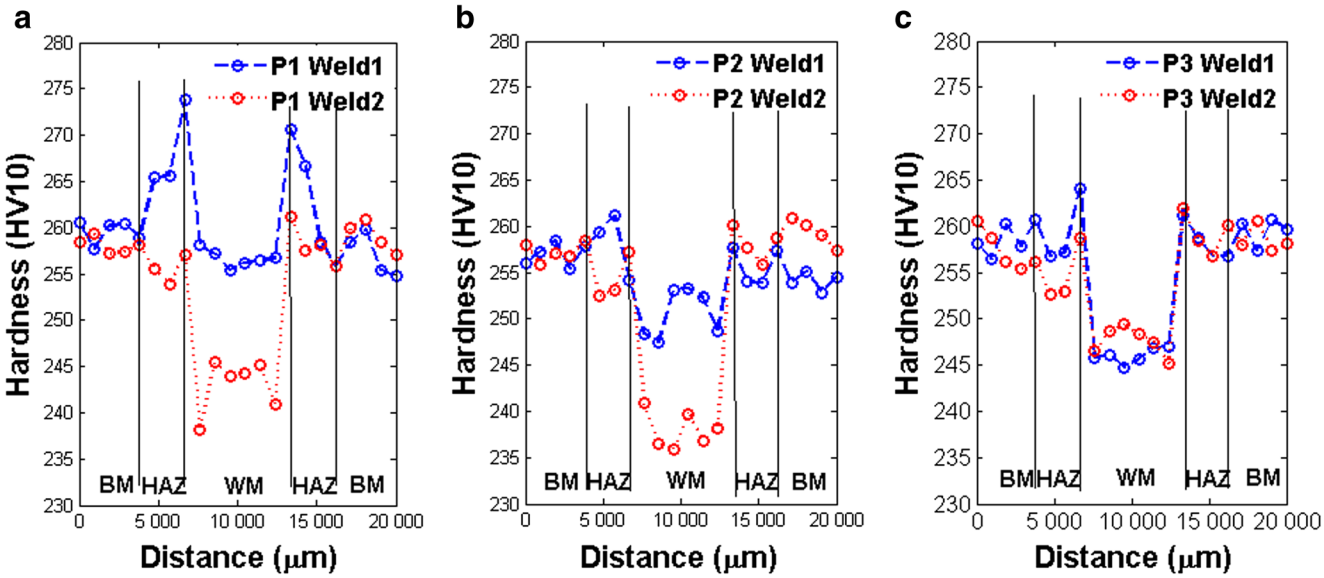

Fig. 12 Hardness profiles across the two weldments in differents area: **a** base metal BM, **b** heat affected zone HAZ and **c** weld metal WM

and some inclusions (Fig. 11f). Consequently, the ferrite phase exhibited a mixed mode of dimple and cleavage or quasi-cleavage [19, 29].

3.3.3 Hardness testing

The hardness evolution in the two welds is shown in Fig. 12. A stable hardness of about 258 HV is observed for the base metal. For the HAZ, the hardness is stable except at the first pass of the first weld, where a peak of hardness (270 HV) is observed. This can be explained by the substitution effect of Cr and Mo [19, 30] and the higher austenite content. The hardness of the deposited metals is lower than that of the base metal and HAZ. The average hardness of the deposited metal employing ER 2594 is higher than that of ER 2209 filler metal and is almost the same as the base metal 253 HV (Fig. 12a).

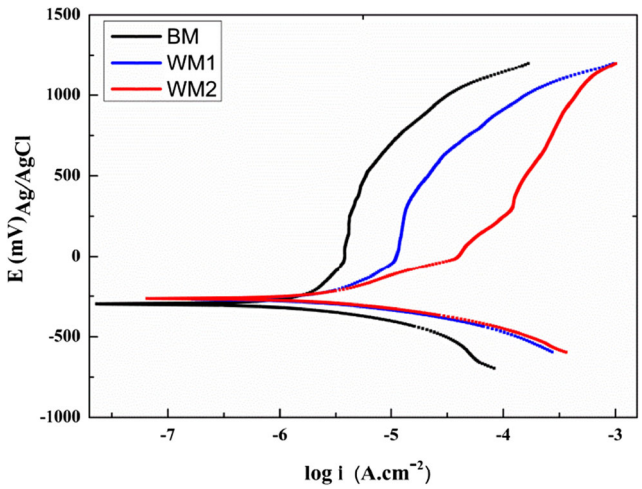

Fig. 13 Potentiodynamic polarization curves of base metal and weld metals in 3.5% NaCl solution at room temperature

Hence, an acceptance stability of the hardness along the profile, also for the second weld, is obtained. It is evident that the root and cap passes have higher hardness than that of the second pass. It is worth to be mentioned that the most stable profile is P2 of the first weld where there is a mixture of two filler metals (Fig. 12b).

3.4 Corrosion behavior

The corrosion susceptibility of base metal and weld metals in 3.5% NaCl solution at room temperature is described by the potentiodynamic polarization curves shown in Fig. 13. From this last, the various electrochemical parameters, the corrosion potential (E_{corr}), the corrosion current density (I_{corr}), and corrosion rate (V_{corr}) are extracted and summarized in Table 5.

Polarization curves reveal clearly the influence of microstructure, for each pass of weld, on the corrosion resistance. It can be observed that the first weld metal shows a corrosion behavior ($I_{corr} = 2.37$ μA/cm^2 and $V_{corr} = 27.75$ μm/y) better than that of the second weld metal ($I_{corr} = 2.60$ μA/cm^2 and $V_{corr} = 30.44$ μm/y). This can be explained by the microstructure, the morphology and finer austenite grains size [5, 31, 32], and the high level of alloying elements such as Cr, Mo, and N in the root pass deposited metal [22, 33, 34]. However,

Table 5 Electrochemical corrosion parameters obtained from potentiodynamic polarization curves of various specimens in 3.5% NaCl solution at room temperature

Sample	BM	WM1	WM2
E_{corr} (mV)	−293.8	−262.5	−263
I_{corr} (μA/cm^2)	1.36	2.37	2.60
V_{corr}(μm/y)	15.92	27.75	30.44

the base metal exhibits the ideal corrosion behavior (I_{corr} = 1.36 μA/cm^2 and V_{corr} = 15.92 μm/y) due to its microstructure and the good equilibrium between austenite/ferrite phases [34].

4 Conclusion

1) The grain sizes of austenite were decreased with increasing of nickel and nitrogen content in the filler metal.
2) The increase of nitrogen content accelerates during cooling the austenite reformation of different morphologies in particular Widmanstätten austenite and limits the welding thermal effect and promotes austenite formation in the heat-affected zone.
3) Mechanical tests demonstrated that the weldment produced by the filler metal combination between ER 2594 in the root pass and ER 2209 in the remaining gives the best tensile and toughness properties better than that produced by ER 2209 for all passes.
4) The hardness test indicates that the most stable profile is the second profile of the first weld where there was a mixture of two deposited metals.
5) The corrosion resistance of the first weld metal is better compared to that of second weld metal, due to finer grains size and morphology of austenite in root pass also the high content of alloying elements such as Cr, Mo, and N.

Acknowledgments The authors wish to express their sincere appreciations to the Research Center in Industrial Technologies (CRTI) and Special thanks to the Laboratory of Science and Materials Engineering (LSGM). The authors would like to thank also the Pr. Moussa SEDRAOUI for their valuable suggestions and comments which helped us to improve this paper.

References

1. Gunn RN (2003) Duplex stainless steels—microstructure, properties and applications. Woodhead Publishing Ltd, Abington Hall, Abington, pp 1–8
2. Armas IA, Moreuil SD (2009) Duplex stainless steels, British Library Cataloguing-in-Publication Data ISTE Ltd, p 47–50
3. Boluta M, Kong CY, Blackburn J, Cashell KA, Hobson PR (2016) Yb-fibre laser welding of 6 mm duplex stainless steel 2205. Phys Procedia 83:417–425. https://doi.org/10.1016/j.phpro.2016.08.043
4. Geng S, Sun J, Guo L, Wang H (2015) Evolution of microstructure and corrosion behavior in 2205 duplex stainless steel GTA-welding joint. J Manuf Process 19:32–37. https://doi.org/10.1016/j.jmapro.2015.03.009
5. Lai R, Cai Y, Wu Y, Li F, Hua X (2016) Influence of absorbed nitrogen on microstructure and corrosion resistance of 2205 duplex stainless steel joint processed by fiber laser welding. J Mater Process Technol 231:397–405. https://doi.org/10.1016/j.jmatprotec.2016.01.016
6. Corolleur A, Fanica A, Passot G (2015) Ferrite content in the heat affected zone of duplex stainless steels. BHM 160(9):413–418. https://doi.org/10.1007/s00501-015-0408-8
7. Muthupandi V, BalaSrinivasan P, Seshadri SK, Sundaresan S (2003) Effect of weld metal chemistry and heat input on the structure and properties of duplex stainless steel welds. Mater Sci Eng A 358(1-2):9–16. https://doi.org/10.1016/S0921-5093(03)00077-7
8. Sridhar R, Ramkumar KD, Arivazhagan N (2014) Characterization of microstructure, strength, and toughness of dissimilar weldments of Inconel 625 and duplex stainless steel SAF 2205. Acta Metall Sin (Engl. Lett.) 27(6):1018–1030. https://doi.org/10.1007/s40195-014-0116-5
9. Jebaraj AV, Ajaykumar L (2013) Influence of microstructural changes on impact toughness of weldment and base metal of duplex stainless steel AISI 2205 for low temperature applications. Procedia Eng 64:456–466. https://doi.org/10.1016/j.proeng.2013.09.119
10. Yousefieh M, Shamanian M, Saatchi A (2011) Influence of heat input in pulsed current GTXW process on microstructure and corrosion resistance of duplex stainless steel welds. J Iron Steel Res Int 18(9):65–69. https://doi.org/10.1016/S1006-706X(12)60036-3
11. Hosseini VA, Bermejo MAV, Gårdstam J, Hurtig K, Karlsson L (2016) Influence of multiple thermal cycles on microstructure of heat-affected zone in TIG-welded super duplex stainless steel. Weld World 60(2):233–246. https://doi.org/10.1007/s40194-016-0300-5
12. Ajith PM, Sathiya P, Aravindan S (2014) Characterization of microstructure, toughness, and chemical composition of friction-welded joints of UNS S32205 duplex stainless steel. Friction 2(1):82–91. https://doi.org/10.1007/s40544-014-0042-6
13. Pekkarinena J, Kujanpääa V (2010) The effects of laser welding parameters on the microstructure of ferritic and duplex stainless steels welds. Phys Procedia 5:517–523. https://doi.org/10.1016/j.phpro.2010.08.175
14. Young MC, Chan SLI, Tsay LW, Shin CS (2005) Hydrogen-enhanced cracking of 2205 duplex stainless steel welds. Mater Chem Phys 91(1):21–27. https://doi.org/10.1016/j.matchemphys.2004.10.042
15. Topolska S, Labanowski J (2015) Impact-toughness investigations of duplex stainless steels. Mater Technol 49(4):481–486. 10.17222/mit.2014.133
16. Juraga I, Stojanović I, Ljubenkov B (2014) Experimental research of the duplex stainless steel welds in shipbuilding. J Nav Archit Shipbuil Indus (Brodogradnja) 65(2):73–85
17. Pilhagen J, Sieurin H, Sandström R (2014) Fracture toughness of a welded super duplex stainless steel. Mater Sci Eng A 606:40–45. https://doi.org/10.1016/j.msea.2014.03.049
18. Ramkumar KD, Mishra D, Thiruvengatam G, Sudharsan SP, Mohan TH, Saxena V, Pandey R, Arivazhagan N (2015) Investigations on the microstructure and mechanical properties of multi-pass PCGTA welding of super-duplex stainless steel. Bull Mater Sci 38(4):1–10. https://doi.org/10.1007/s12034-015-0915-y
19. Kang DH, Lee HW (2012) Effect of different chromium additions on the microstructure and mechanical properties of multipass weld joint of duplex stainless steel. Metall Mater Trans A 43(12):4678–4687. https://doi.org/10.1007/s11661-012-1310-6
20. Muthupandi V, Srinivasan PB, Shankar V, Seshadri SK, Sundaresan S (2005) Effect of nickel and nitrogen addition on the microstructure and mechanical properties of power beam processed duplex stainless steel (UNS 31803) weld metals. Mater Lett 59(18):2305–2309. https://doi.org/10.1016/j.matlet.2005.03.010
21. Pilhagen J, Sandström R (2014) Influence of nickel on the toughness of lean duplex stainless steel welds. Mater Sci Eng A 602:49–57. https://doi.org/10.1016/j.msea.2014.01.093
22. Eghlimi A, Shamanian M, Raeissi K (2014) Effect of current type on microstructure and corrosion resistance of super duplex stainless steel claddings produced by the gas tungsten arc welding process.

Surf Coat Technol 244:45–51. https://doi.org/10.1016/j.surfcoat.2014.01.047
23. Zhang Z, Jing H, Xu L, Han Y, Zhao L (2016) Investigation on microstructure evolution and properties of duplex stainless steel joint multi-pass welded by using different methods. Mater Des 109:670–685. https://doi.org/10.1016/j.matdes.2016.07.110
24. Ogawa T, Koseki T (1989) Effect of composition profiles on metallurgy and corrosion behavior of duplex stainless steel weld metals. Weld J 68(5):181–191
25. Liou HY, Hsieh RI, Tsai WT (2002) Microstructure and stress corrosion cracking in simulated heat-affected zones of duplex stainless steels. Corros Sci 44(12):2841–2856. https://doi.org/10.1016/S0010-938X(02)00068-9
26. Wang HS (2005) Effect of welding variables on cooling rate and pitting corrosion resistance in super duplex stainless weldments. Mater Trans 46(3):593–601. https://doi.org/10.2320/matertrans.46.593
27. Ramkumar KD, Thiruvengatam G, Sudharsan SP, Mishra D, Arivazhagan N, Sridhar R (2014) Characterization of weld strength and impact toughness in the multi-pass welding of super-duplex stainless steel UNS 32750. Mater Des 60:125–135. https://doi.org/10.1016/j.matdes.2014.03.031
28. de Lacerda JC, Cândido LC, Godefroid LB (2015) Effect of volume fraction of phases and precipitates on the mechanical behavior of UNS S31803 duplex stainless steel. Int J Fatigue 74:81–87. https://doi.org/10.1016/j.ijfatigue.2014.12.015
29. Zhang Z, Jing H, Xu L, Han Y, Li G, Zhao L (2017) Investigation on microstructure and impact toughness of different zones in duplex stainless steel welding joint. J Mater Eng Perform 26(1):134–150. https://doi.org/10.1007/s11665-016-2441-5
30. Belkessa B, Miroud D, Ouali N, Cheniti B (2016) Microstructure and mechanical behavior in dissimilar SAF2205/API X52 welded pipes. Acta Metall Sin (Engl Lett) 29(7):674–682. https://doi.org/10.1007/s40195-016-0428-8
31. Heping L, Xuejun J, Wuhan J (2011) Electrochemical corrosion behavior of the laser continuous heat treatment welded joints of 2205 duplex stainless steel. Univ Technol Mater Sci Ed 26(6):1140–1147. https://doi.org/10.1007/s11595-011-0378-y
32. Neissi R, Shamanian M, Hajihashemi M (2016) The effect of constant and pulsed current gas tungsten arc welding on joint properties of 2205 duplex stainless steel to 316L austenitic stainless steel. J Mater Eng Perform 25(5):2017–2028. https://doi.org/10.1007/s11665-016-2033-4
33. Ma L, Hu S, Shen J (2017) Microstructure, properties and weldability of duplex stainless steel 2101. J Mater Eng Perform 26(1):250–257. https://doi.org/10.1007/s11665-016-2428-2
34. Atapour M, Sarlak H, Esmailzadeh M (2016) Pitting corrosion susceptibility of friction stir welded lean duplex stainless steel joints. Int J Adv Manuf Technol 83(5-8):721–728. https://doi.org/10.1007/s00170-015-7601-5